INORGANIC CHEMISTRY FRONTIERS

RESEARCH ARTICLE

View Article Online
View Journal | View Issue

Cite this: *Inorg. Chem. Front.*, 2025, **12**, 8260

Dual-modulation of lanthanide valence and MOF phase transition: advancing ratiometric thermometry in Eu-doped ZIF-L films for high-sensitivity thermal sensing

Jiayu Zheng,[a] Longxiao Zhou,[a] Qiufen Liu,[a] Senwei Wu,[a] Yuting Peng,[a] Xiujian Zhao [a] and Shouqin Tian *[a,b]

Received 4th June 2025,
Accepted 9th August 2025

DOI: 10.1039/d5qi01248a

rsc.li/frontiers-inorganic

Ratiometric optical thermometry has emerged as a vital platform for non-contact temperature monitoring in industrial and scientific applications, demanding sensors with high sensitivity, non-invasiveness, and spatial resolution. Although zeolitic imidazolate framework-8 (ZIF-8) possesses attractive thermal stability and structural tunability, its limited luminescence intensity hinders practical thermometric applications. Meanwhile, ZIF-L, a two-dimensional (2D) polymorph of ZIF-8 with identical ligands, remains unexplored for temperature sensing. Herein, we propose a dual-modulation strategy synergizing lanthanide valence engineering with MOF phase control to develop a multi-emission center Eu^{3+}/Eu^{2+} co-doped ZIF-L film (Eu/ZIF-L). By introducing Eu^{3+} into ZIF-8 precursors, the partial reduction of Eu^{3+} to Eu^{2+} under thermal treatment triggers a structural evolution from 3D ZIF-8 to 2D ZIF-L. The resultant Eu/ZIF-L exhibits dual emission peaks at 450 nm (Eu^{2+}) and 495 nm (ligand-centered), with their intensity ratio (I_{495}/I_{450}) demonstrating remarkable linear temperature dependence over 296–373 K and achieving a relative sensitivity of 1.95% K^{-1}. This work pioneers the integration of valence-state manipulation and MOF phase transition for thermometric optimization, providing a novel paradigm to design advanced ratiometric MOF thermometers for industrial thermal management.

1. Introduction

Temperature (T), as a fundamental physical parameter, is intrinsically linked to virtually all physical and chemical processes. Precise non-contact temperature measurement plays a crucial role in diverse scientific research and industrial production fields, demanding enhanced requirements for temperature sensor accuracy and sensitivity.[1] Luminescent thermometers, empowered by non-contact optical thermometry techniques, have achieved high spatial resolution, superior sensitivity, and remote monitoring capabilities, demonstrating promising applications in biomedical engineering, chemical synthesis, and environmental surveillance.[2,3] Furthermore, ratiometric thermometers exhibit distinctive advantages, including self-calibration capability, rapid response time, high precision, and broad applicability, establishing them as the most extensively studied and applied temperature measurement technology within optical thermometry.[4–6] Current characterization strategies for thermal sensing performance primarily involve tracking spectral shifts, fluorescence lifetime variations, intensity modulations, or fluorescence intensity ratio (FIR) evolution.

To date, diverse materials have been developed as optical ratiometric thermometers, including polymers, rare earth ion (Ln)-based phosphors, quantum dots (or nanocrystals), and metal organic frameworks (MOFs).[7–11] MOFs, with their tunable metal nodes, organic linkers, and guest species, offer vast structural diversity that creates expansive opportunities for fluorescence applications.[12–14] Lanthanide luminescent materials have emerged as ideal guest species in MOFs due to their tunable emission characteristics and versatile energy transfer processes.[15,16] By synergistically combining the luminescence of lanthanide elements (Ln) with the advantages of porous frameworks, dual/multi-emission lanthanide-incorporated MOFs (Ln-MOFs) demonstrate exceptional thermometric characteristics, showing promising potential for ratiometric thermometry applications.[17–19]

Zeolite imidazole frameworks (ZIFs), a class of MOFs, are constructed from imidazolate ligands and tetrahedral metal ions (*e.g.*, Zn^{2+} and Co^{2+}) through coordination.[20] ZIF-8 (Zn$(mim)_2$) as a typical ZIF is composed of Zn^{2+} coordinated with

[a]*State Key Laboratory of Silicate Materials for Architectures, Wuhan University of Technology (WUT), No. 122, Luoshi Road, Wuhan 430070, P. R. China*
[b]*State Key Laboratory of Advanced Glass Materials, WUT, No. 122, Luoshi Road, Wuhan 430070, P. R. China*

deprotonated 2-methylimidazole (Hmim) *i.e.* mim- to form a 3dimensional (3D) sodalite topology (SOD). According to previous reports, ZIF-8 has been paid more attention by researchers due to its large specific surface area, high thermal stability and facile functionalization.[21–23] In addition, ZIF-L (Zn(mim)$_2$·(Hmim)$_{1/2}$·H$_2$O$_{3/2}$) with 2D structures has the same coordination structure unit as ZIF-8, whose structure is stabilized by the intertwining layers of the ligated unsaturated Hmim and free Hmim molecules through hydrogen bonding. As a structural analog of ZIF-8, ZIF-L possesses a unique layered two-dimensional structure and demonstrates excellent chemical and thermal stability, which has been extensively investigated in fields such as catalysis, gas adsorption, and fluorescent probes.[24] Compared with three-dimensional architectures, this two-dimensional configuration endows ZIF-L with enhanced superior structural flexibility and exposed active sites, making it an ideal candidate for dynamic photophysical applications.[25] Notably, while addressing the critical challenge of ZIF-8's inherent fluorescence weakness in temperature sensing applications, we propose that ZIF-L's larger specific surface area and abundant adsorption sites could significantly enhance temperature detection sensitivity, potentially expanding the practicality of MOF-based luminescent thermometers.

Herein, we developed a novel europium ion (Eu^{3+}/Eu^{2+})-doped ZIF-L (Eu/ZIF-L) multi-emissive film *via* a facile sol–gel approach, demonstrating fluorescence intensity ratio (FIR)-based thermometric capability with exceptional potential for non-contact temperature sensing. The structural transformation and the formation process of the emission centers are illustrated in Scheme 1. The tripartite emission centers arise from the imidazolate ligands (450 nm) in the ZIF-L framework, the intense narrow-band Eu^{2+} emission (495 nm), and the subdued Eu^{3+} red luminescence (618 nm). Surprisingly, a dimensionality transition from 3D ZIF-8 to 2D ZIF-L was triggered by modulating the Eu(NO$_3$)$_3$·6H$_2$O concentration in the composite sol. Thermal activation induces partial reduction of Eu^{3+} to Eu^{2+}, with the latter exhibiting sharpened and intensified emission attributed to the ligand-to-metal antenna effect *via* Eu^{2+}–N coordination in the ZIF-L matrix. Crucially, across a wide operational window (296–373 K), the dual emission bands (450 nm and 495 nm) and their intensity ratio display robust linear thermal responsiveness (R^2 = 0.976), achieving a relative thermometric sensitivity of 1.95% K^{-1} at 363 K. Following this, the Eu/ZIF-L film with a good reversible fluorescence thermal response performance has application prospects in ratiometric temperature-sensing.

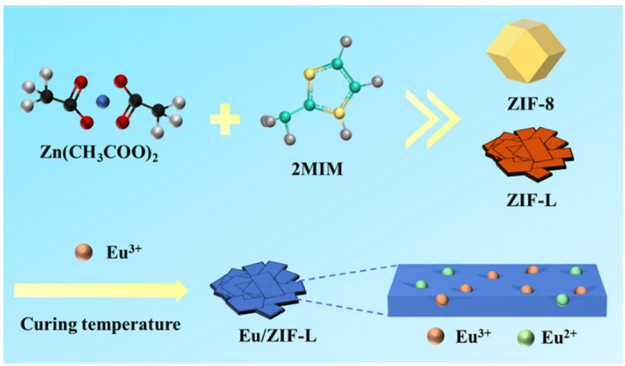

Scheme 1 Diagram of the multi-emission center Eu^{3+}/Eu^{2+} co-doped ZIF-L film.

2. Experimental sections

2.1. Materials

Zinc(II) acetate dihydrate (Zn(CH$_3$COO)$_2$·2H$_2$O, ≥99.9%, Shanghai China), 2-methylimidazole (Hmim, C$_4$H$_6$N$_2$, 99%, Aladdin), ethanol (C$_2$H$_5$OH, ≥99.7%, Shanghai China), and europium(III) nitrate hexahydrate (Eu(NO$_3$)$_3$·6H$_2$O, 99.9%, Macklin)were used; all reagents were directly used without further purification.

2.2. Preparation of Eu/ZIF-L films

The specific preparation process was as follows. Firstly, Hmim (0.05 mol) and zinc acetate dihydrate (0.01 mol) were mixed in 2 mL of ethanol, and then stirred at room temperature to form transparent ZIF sols. 3 mL of the ZIF sol was taken in a small bottle and 0.4 mmol Eu(NO$_3$)$_3$·6H$_2$O was added into the bottle with continuous stirring to form a transparent composite sol. (The concentration of Eu salts was 0.133 mol L^{-1} serving the ZIF sol as solvents.) After that, the composite sol was coated on a clear quartz glass through a spin-coating method and the wet Eu/ZIF film was obtained. And the wet film was taken on a hot plate for heat treatment. The specific procedure of heat treatment was to hold at 70 °C for half an hour and raise the temperature to 80 °C firstly, then heat up to 90 °C at a rate of 10 °C h^{-1} and hold for an hour. After that, the temperature was increased at a rate of 20 °C h^{-1} to 100 °C and maintained for 5 h. Finally, the Eu/ZIF-L film was obtained. On the other hand, the amount of Eu salts in Eu/ZIF-L films could be controlled by changing the concentration of Eu(NO$_3$)$_3$·6H$_2$O in the composite sol.

2.3. Characterization

The phase structure of the film samples was characterized using an X-ray diffractometer (GIXRD, Empyream) with grazing incidence. Its X-ray source was 4 kW Cu Kα (λ = 1.5418 Å) radiation, with a scanning speed of 0.02° 2θ s^{-1} and a test range of 5°–60°. A field emission scanning electron microscope equipped with X-Max 50 X-ray energy dispersive spectrometer (FESEM-EDS, Zeiss Ultra Plus) was used to analyze the morphology and microstructure of the prepared films. Its secondary electron resolution was 1.0 nm (15 kV) and 1.2 nm (1 kV), the acceleration voltage was 0.02–30 kV, and the resolution of the energy dispersive spectrometer at Mn Kα was better than that at 127 eV. A Fourier transform infrared spectrometer (FTIR, Nicolet 6700) was used to detect the characteristic infrared vibration peaks in the microstructure of the films to observe the changes of the film structure. The detection wavenumber range was 4000–400 cm^{-1} (mid-infrared region), with a fast scanning speed of 1 time per second and a maximum

resolution of 0.019 cm^{-1}. The changes in the surface structure of the films were tested by X-ray photoelectron spectrometer (XPS, ESCALAB 250Xi, ThermoFisher), with an energy scanning range of 0–5000 eV. The UV-visible absorption spectra of the films were tested by UV-visible-NIR spectrophotometer (UV-3600, SHIMADZU), with a test wavelength range of 300–2500 nm and a scanning step of 1 nm. At room temperature, the photoluminescence (PL) and photoluminescence excitation (PLE) spectra of all films were recorded using a fluorescence spectrophotometer (TRFS, QM/TM/NIR, USA). The steady-state part of its light source was a 75 W xenon lamp; the transient part was a tunable picosecond laser, with a signal-to-noise ratio of 6000 : 1 (up to 10 000 : 1). The thermal response fluorescence of the films was detected using thermal sensing accessories, which could record the temperature-dependent fluorescence spectra of the film samples and calculate the corresponding relative sensitivity. The fluorescence decay curves of the samples were measured using a time-resolved fluorescence spectrometer (Newport, USA) with a resolution of 100–400 fs, and the fluorescence lifetime and time resolution were obtained by fitting the test results.

3. Results and discussion

3.1. Structural characterization

We analyzed the physical structure of the obtained ZIF films before/after Eu-modified, as shown in the XRD pattern of Fig. 1. It can be seen that the film prepared with the ZIF sol without $Eu(NO_3)_3{\cdot}6H_2O$ was ZIF-8, consistent in the CCDC data base numbered CCDC 602542.[26,27] However, after adding $Eu(NO_3)_3{\cdot}6H_2O$ into the ZIF sol, the ZIF-L (CCDC 1509273) film was obtained,[28] indicating that the addition of Eu ions promoted the transformation from ZIF-8 to ZIF-L. (The chemical formulas of ZIF-8 and ZIF-L are $Zn(mim)_2$ and $Zn(mim)_2{\cdot}(Hmim)_{1/2}{\cdot}H_2O_{3/2}$, respectively, in which mim represents deprotonated 2-methylimidazole.[29]) The possible reason for this phenomenon was a small amount of Eu ions coordinated with Hmim resulting in changes of the growth direction of ZIFs from three dimensional (3D) ZIF-8 structures to two dimensional (2D) ZIF-L.

Based on the diffraction data in Fig. 1, we calculated the lattice parameters of ZIF-8 ($a = b = c = 17.03$ Å, $\beta = 90°$) and the lattice parameters of ZIF-L with Eu ($a = 24.00$ Å, $b = 17.68$ Å, $c = 19.8$ Å, $\beta = 90°$), these calculated results agree well with the standard cards (CCDC 602542, $a = b = c = 16.99$ Å; CCDC 1509273, $a = 24.12$ Å, $b = 17.06$ Å, $c = 19.74$ Å) respectively.

In order to observe the morphologies of the ZIF-8 film and the Eu/ZIF-L film, FESEM characterization was carried out as shown in Fig. 2. It can be seen from Fig. 2a that there were particles with sizes of ~10 μm on the surface of the ZIF-8 film and the morphology of particles was cubes without sharp corners. In contrast, the thickness was ~3.34 μm (Fig. 2c). In Fig. 2b, a lot of well-defined square blocks with a relatively uniform size of ~4 μm were observed, speculating that the shape was formed due to the stacking of lamellar structures. Numerous lamellar structures were stacked irregularly together and the thickness was up to 4.31 μm (Fig. 2d), it further indicated that the transformation from 3D ZIF-8 to 2D ZIF-L can be achieved through introducing Eu salts into the ZIF sol. As expected, EDS results (Fig. 2e and f) showed that Eu elements existed in the ZIF-L film with an obviously increased relative intensity of O elements compared to the ZIF-8 film, suggesting that the Eu/ZIF-L film was successfully synthesized.

To investigate the structural difference between the ZIF-8 film and the Eu/ZIF-L film, we performed FTIR characteriz-

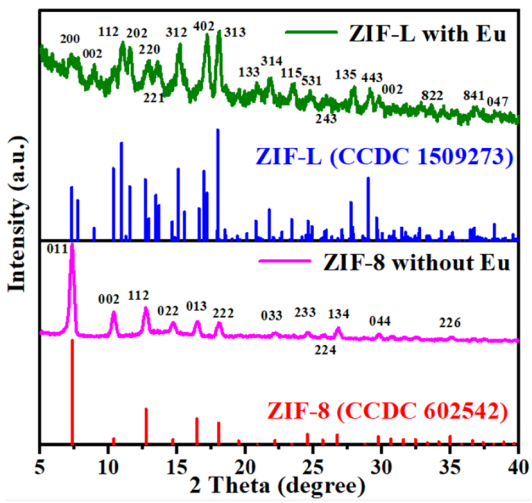

Fig. 1 XRD patterns of the ZIF-8 film without Eu and the Eu/ZIF-L film.

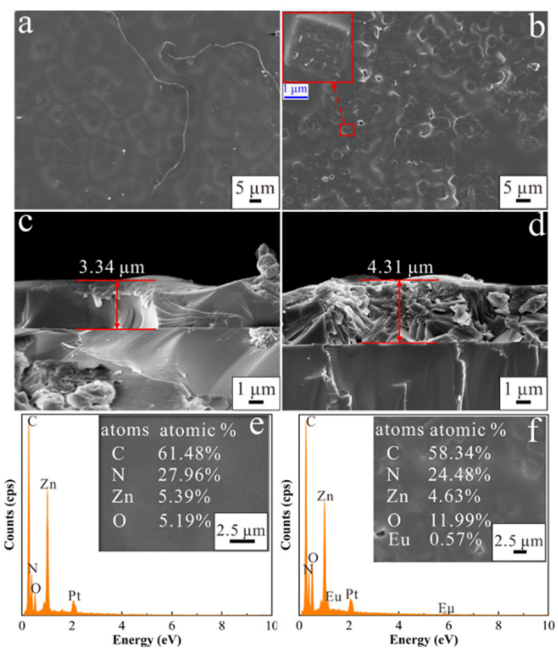

Fig. 2 Top-view (a and b) and side-view (c and d) FESEM images and EDS spectra (e and f) of the ZIF-8 film (a, c and e) and the Eu/ZIF-L film (b, d and f).

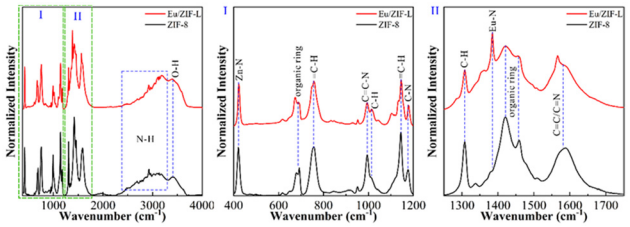

Fig. 3 FTIR spectra of ZIF-8 and Eu/ZIF-L films. The enlarged IR spectra in the range from 1200 to 400 cm^{-1} (I), from 1750 to 1250 cm^{-1} (II).

ation as shown in Fig. 3 and Table S1. Since the coordination unites of ZIF-8 and ZIF-L are almost consistent, most of bonds exhibited the same IR spectral absorptions, as shown in Table S1. It is noted that a new infrared absorption peak centered at 1384 cm^{-1} appeared in the Eu/ZIF-L film (Fig. 3II), which was attributed to the vibration of Eu–N.[30,31] However, no peaks could be observed in the ZIF-8 film, indicating the formation of Eu–N bonds after introducing Eu salts. Therefore, some Eu ions have been successfully coordinated with the N active site on the imidazole ligands in the ZIF-L skeleton.

In order to further investigate differences in surface structures between the ZIF-8 film and the Eu/ZIF-L film, XPS characterization was performed as shown in Fig. 4. Fig. 4a shows the presence of Eu, C, N, O and Zn elements in the Eu/ZIF-L film and C, N, O and Zn elements existed in the ZIF-8 film. In addition, high-resolution XPS spectra of C 1s both in the ZIF-8 film (Fig. 4d) and the Eu/ZIF-L film (Fig. 4g) were deconvoluted into four peaks centered at ~284.8, ~285.6, ~286.6 and ~288.5 eV, mainly corresponding to C-sp^3, C=C, C–N and C=N in Hmim ligands, respectively[32,33] (there would be some amorphous carbon due to the need for testing). And

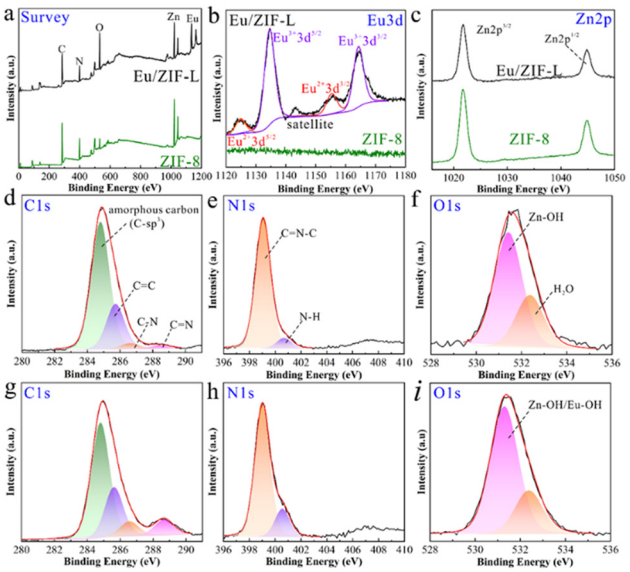

Fig. 4 XPS survey spectra (a), high resolution Eu 3d (b), Zn 2p (c), C 1s (d and g), N 1s (e and h), and O 1s (f and i) spectra of the ZIF-8 film (a–f) and the Eu/ZIF-L film (a–c and g–i).

it can be seen that the relative intensity of C–N and C=N in the Eu/ZIF-L film was obviously higher than that in the ZIF-8 film since more organic ligands participated in forming the ZIF-L framework. Moreover, high resolution N 1s spectra (Fig. 4e and h) show two peaks at ~399.0 and ~400.1 eV corresponding to C=N–C and N–H, respectively. Since the layers are connected with each other using free 2-methelimidazole molecules by hydrogen bonding interactions in ZIF-L frameworks,[28] as expected, the relative intensity of protonated N (N–H) in Eu/ZIF-L was higher than that in ZIF-8. On the other hand, high-resolution Eu 3d spectrum of the Eu-modified ZIF-L film was deconvoluted into five peaks (Fig. 4b). In the Eu/ZIF-L film, two peaks at ~1134.5 and ~1164.3 eV were attributed to Eu^{3+} and another two peaks centered at ~1124.7 and ~1155.3 eV were related to Eu^{2+}, which was from the surface layer, called the "surface valence transition".[34–36] However, no peaks can be seen in the ZIF-8 film (Fig. 4b). And XPS high resolution Zn 2p spectra (Fig. 4c) were composed of two peaks centered at ~1021.8 and ~1044.8 eV, consistent with binding energies of Zn $2p^{3/2}$ and Zn $2p^{1/2}$, respectively, indicating the existence of Zn^{2+} both in the ZIF-8 film and the Eu/ZIF-L film.[37] In Fig. 4f and i, high-resolution O 1s spectra were fitted into two peaks. A peak at ~531.6 eV was assigned to Zn–OH groups and another peak at ~532.7 eV was attributed to H_2O molecules, suggesting that there were extra oxygen atoms bonding with unsaturated Zn defects in the form of hydroxyl groups both in the ZIF-8 film and the Eu/ZIF-L film.[38,39] It was noteworthy that unsaturated Eu sites (*i.e.* Eu–OH) may exist in the Eu/ZIF-L film due to the involvement of Eu ions in the formation of the ZIF-L structure (Fig. 3II). In this sense, the transformation from ZIF-8 to ZIF-L may be related to Eu ions, and further testing and characterization is required to verify the valence of such Eu ions.

To explore the reason for the phase structure transformation from ZIF-8 to ZIF-L after introducing Eu salts, a series of Eu/ZIF films with different concentrations of Eu salts were synthesized and characterized by XRD as shown in Fig. S1. It can be seen from the figure that the ZIF-8 structure was obtained when the concentration of Eu was not more than 0.017 mol L^{-1}. Obviously, a small bulge appeared at ~17.2° ((402) facet) as the concentration of Eu salts was 0.033 mol L^{-1}, however, the phase structure was still ZIF-8. When the concentration of Eu salts was up to 0.067 mol L^{-1}, characteristic diffraction peaks originating from ZIF-L was obvious. Additionally, the phase structure of ZIF-L was still maintained as continuing increasing the concentration of Eu salts. Since the 2D layers in the ZIF-L stacking along the *c* direction are part of the sodalite topology in the 3D structure of ZIF-8.[40] Moreover, metal Eu ions can serve as a metal source to coordinate with organic imidazole ligands in the form of Eu^{2+}.[41,42] In this sense, it was likely due to the phase transformation, that a small amount of Zn^{2+} was replaced by Eu^{2+} forming coordination bonds between Eu^{2+} and the N active site in 2-methylimidazole, leading to the change of the growth direction of the ZIF framework. However, the ability of Eu^{2+} in the system to participate in coordination is closely related to the amount of Eu salts

added to the ZIF sol and the amount of Eu^{2+} produced by the "surface valence transition".

In addition, we mixed Hmim and $Eu(NO_3)_3{\cdot}6H_2O$ in ethanol in a 2 : 1 molar ratio at room temperature to investigate whether there would be a reaction between them. The experimental phenomenon indicated that the two reagents could react rapidly to form white precipitates, the precipitates were dried and characterized by FTIR and XPS, and the results obtained are shown in Fig. S2. It can be seen in Fig. S2a that there were Eu–O and Eu–N infrared absorption peaks, indicating the reaction can occur at room temperature. Moreover, Eu 3d spectra (Fig. S2c) showed that almost no peaks of Eu^{2+} were present, and the relative intensities of NO_3^- and N–H in N 1s (Fig. S2e) were obviously higher than that of C=N–C. These results suggest that $Eu(NO_3)_3{\cdot}6H_2O$ can react with Hmim at room temperature in the absence of zinc salts, while the reaction is incomplete and almost all metal ions coordinated to N sites from Hmim are Eu^{3+} rather than Eu^{2+}.

We propose that the structural transition from ZIF-8 to ZIF-L is not only related to the doped Eu^{3+} but also significantly influenced by the curing temperature. This phenomenon is consistent with relevant research findings, where, for instance, researchers observed that the phase transition of $LiYO_2$ is closely associated with both Yb^{3+} concentration and temperature when Yb^{3+} is doped into the $LiYO_2$ matrix.[43] In order to explore the source of Eu^{2+} produced in the Eu/ZIF-L film, FTIR was performed on the Eu/ZIF sol and films cured at different temperatures and the results are shown in Fig. S3. In Fig. S3II, no infrared absorption peak of Eu–N was observed in the Eu/ZIF sol in the presence of Zn^{2+}, indicating that the Eu^{3+} coordination with Hmim was suppressed. Additionally, the relative intensity of the Eu–N peak at 1384 cm^{-1} was enhanced as the curing temperature increased. Furthermore, Fig. 4b shows the apparent presence of Eu^{2+} in the well-cured Eu/ZIF-L film, implying that the production of Eu^{2+} was closely related to the curing temperature.

To further understand the trend of the content of Eu ions used for the formation of the ZIF-L skeleton in Eu/ZIF-L films, FTIR (Fig. S4) and high-resolution XPS spectra of Eu 3d (Fig. S5a) and N 1s (Fig. S5b) in Eu/ZIF films synthesized with different initial concentrations of $Eu(NO_3)_3{\cdot}6H_2O$ were carried out. It can be seen that the intensities of imidazole ligand-related IR vibrational peaks in Fig. S4 were decreased with the increase of the content of Eu salts. Moreover, the relative intensity of the Eu–N peak centered at 1384 cm^{-1} exhibited a trend of first increase then decrease and the maximum intensity was reached when the concentration of $Eu(NO_3)_3{\cdot}6H_2O$ was 0.133 mol L^{-1}, suggesting that the content of Eu ions involved in the formation of ZIF-L frameworks was up to saturation. Also, it can be seen from Fig. S5a that the relative proportion of Eu^{2+} decreased with the increasing of Eu contents in the synthesized reaction system, indicating that the addition of more Eu salts in the ZIF sol may not be beneficial for the surface valence transition of Eu^{3+}. Furthermore, Table S2 shows that the mole ratio of Eu/Zn on the surface of the ZIF@0.133 mol L^{-1} Eu sample was higher than that of the other samples, demonstrating that the content of Eu^{2+} produced by the Eu^{3+} transition was relatively higher, which would be more favorable for coordination with 2-methylimidazole ligands. Additionally, it can be seen from Fig. S5b that a fitted peak at ~407.0 eV for the sample (ZIF@0.333 mol L^{-1} Eu) was obvious, corresponding to NO_3^-.[44] And the relative intensity of the peak at ~532.7 eV fitted from O 1s in Fig. S4d was obviously increased compared to other samples, indicating the existence of more Eu(III) compound, *i.e.* $Eu(NO_3)_3$ on the surface of the ZIF@0.333 mol L^{-1} Eu sample.[45]

In a word, the phenomenon about "surface valence transition" from Eu^{3+} to Eu^{2+} can occur through controlling the curing temperature in Eu/ZIF films, to achieve the transformation from 3D ZIF-8 to 2D ZIF-L, a possible explanation for the result is that, a small amount of Eu^{2+} is involved in the formation of ZIF frameworks and affects the growth direction of ZIF, which eventually forms ZIF-L structures.

3.2. Photoluminescence performances

To study the luminescence properties of the Eu/ZIF-L film, firstly, the UV-Vis absorption spectra about the ZIF-8 film and the Eu/ZIF-L film (*i.e.* the sample of ZIF@0.133 mol L^{-1} Eu) were recorded as shown in Fig. S6. It can be seen that both the ZIF-8 film and the Eu/ZIF-L film exhibited an absorption edge of ~240 nm because of their same coordinated structures, which was consistent with a previous report.[29] And the excitation and emission spectra of ZIF-8 and Eu/ZIF-L at room temperature are shown in Fig. 5. When the films were excited at 365 nm, linker-based fluorescence could be observed at ~450 nm both in ZIF-8 and Eu/ZIF-L.[46] Additionally, Eu/ZIF-L showed the characteristic emission bands of Eu^{3+} at λ = 595 and 618 nm, which was attributed to $^5D_0 \rightarrow {}^7F_1$ and $^5D_0 \rightarrow {}^7F_2$ of the Eu^{3+} ion, respectively.[47] However, other characteristic emission peaks of Eu^{3+} were too weak to be observed. Surprisingly, a strong narrow emission peak at 495 nm appeared, corresponding to the fluorescence emission of Eu^{2+} due to a d–f transition, which was affected by the coordination environment,[41,48] which was well consistent with the above analysis in Fig. 4b and S3. As for the formation of strong fluorescence originating from Eu^{2+}, the most possible reason was the antenna effect, in which the luminescence from linkers (like the 2-methylimidazole linker) can involve charge transfer with coordinated metal ions (like Eu^{2+}) or clusters.[49]

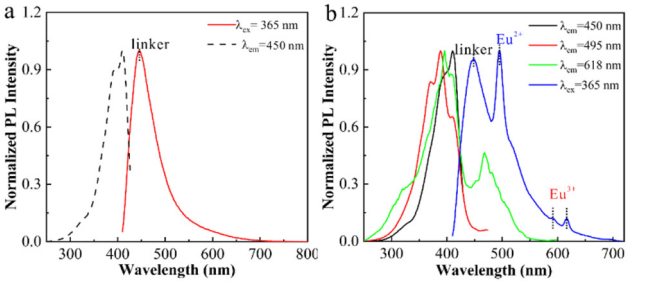

Fig. 5 PL and PLE spectra of the ZIF-8 film (a) and the Eu/ZIF-L film (b).

In order to demonstrate origins of these fluorescence peaks in the Eu/ZIF-L film, PL and PLE spectra of luminescent reactants including $Eu(NO_3)_3{\cdot}6H_2O$ and Hmim ligands in solid and solution states were performed at room temperature as shown in Fig. S7a–d. It can be seen from the result that the fluorescence of Eu^{3+} and ZIF-L frameworks in the Eu/ZIF-L film was consistent with $Eu(NO_3)_3{\cdot}6H_2O$ and Hmim, respectively. Nevertheless, the fluorescence peak at 495 nm in the Eu/ZIF-L film was not observed both in $Eu(NO_3)_3{\cdot}6H_2O$ and Hmim. Additionally, the white precipitate and supernatant obtained from the mixture of Hmim and $Eu(NO_3)_3{\cdot}6H_2O$ with a mole ratio of 2 : 1 were tested by fluorescence spectroscopy, and the results in Fig. S7e and S7f show that there also the fluorescence peak was absent. These results indicated that the fluorescence peak at 495 nm was generated during the preparation of the Eu/ZIF-L film and did not originate from Eu^{3+}.

To further demonstrate that the appearance of the fluorescence peak is related to the curing temperature, PL spectra of Eu/ZIF sols synthesized with different concentrations of Eu salts and the Eu/ZIF-L films (0.133 mol L^{-1} Eu salts) cured at different temperatures were recorded, as shown in Fig. 5.

It was inferred from Fig. S8a that the coordination degree between Zn^{2+} and Hmim was very low due to the high dispersion of reactants in the Eu/ZIF sol. And combined with the fluorescence peak of the Hmim ligand (Fig. S7c and d), it indicated that the fluorescence peak observed at ~450 nm in all sols was caused by the formation of metal complexes with low coordination degree and Hmim ligands. Moreover, the emission peak at 495 nm was not observed in all Eu/ZIF sols, indicating that the formation of the peak was not directly related to the concentration of Eu salts in Eu/ZIF sols. At the same time, the data in Fig. S8a were normalized to obtain Fig. S8b. It is noteworthy that the emission peak (618 nm) of Eu^{3+} increased gradually with the increase of the Eu salt concentration in the Eu/ZIF sol, which further proved that Eu^{3+} was hardly reduced to Eu^{2+} under the chemical environment in the sol. On the other hand, PL spectra of Eu/ZIF-L films (0.133 mol L^{-1} of Eu salts) cured at different temperatures (Fig. S8c and d) show that the emission peak at 495 nm was more and more obvious with the increase of curing temperature, demonstrating that the curing temperature is the key to generate Eu^{2+}.

To further verify that the fluorescence peak at 495 nm originated from Eu^{2+}, we also calculated the fluorescence lifetimes of ZIF-8 and Eu/ZIF-L films, as shown in Fig. 6. The average fluorescence lifetime of ZIF-8 was shown to be 2.56 ns by biexponential fitting (Fig. 6a), whereas the average fluorescence lifetime of the fluorescence emission peak (450 nm) originating from ZIF-L in the Eu/ZIF-L membrane was 1.97 ns (Fig. 6b), this was shorter than that in ZIF-8, and the cause of this phenomenon might be that the photon energy in the ZIF-L framework (based on the ligand) is partially transferred to Eu^{2+} involved in coordination, which makes its fluorescence lifetime shorter. In addition, the fluorescence lifetimes measured when monitoring the fluorescence peaks at 495 nm and 618 nm were calculated by fitting the average lifetimes to

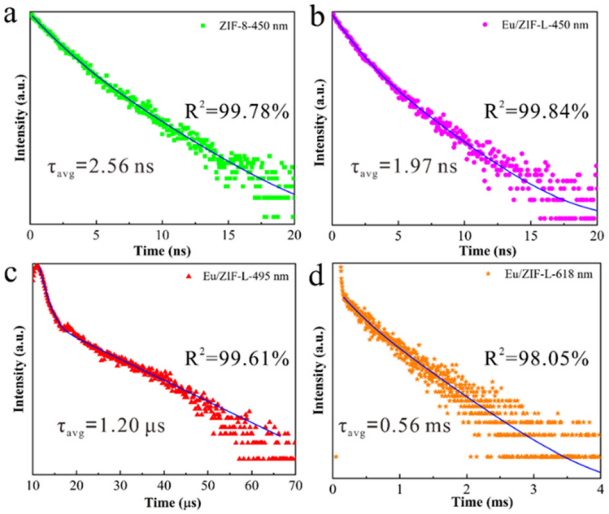

Fig. 6 The fluorescence decay curve at 450 nm for the ZIF-8 film (a) and fluorescence decay curves for the Eu/ZIF-L film monitored at 450 nm (b), 495 nm (c) and 618 nm (d), respectively.

be 1.20 μs (Fig. 6c) and 0.56 ms (Fig. 6d), which were in agreement with the fluorescence lifetimes of Eu^{2+} and Eu^{3+}, respectively,[30,50,51] further confirming that the fluorescence peak at 495 nm originated from Eu^{2+}.

3.3. Temperature sensing performance

To investigate the dependence of fluorescence of the Eu/ZIF-L film on temperature, temperature (T)-dependent fluorescence was recorded in the range of room temperature (23 °C)–100 °C. Prior to the test, excitation wavelength-dependent fluorescence spectra were recorded to select an appropriate excitation wavelength and the result is shown in Fig. 7.

Considering the signal intensity of the main fluorescence peaks (450 and 495 nm) in the Eu/ZIF-L film, an excitation wavelength of 360 nm was chosen for the high-temperature fluorescence measurement. As shown in Fig. 8a, thermal quenching of the emission peaks at 450 and 495 nm occurred when the temperature was increased from room temperature to 100 °C. Additionally, the intensity of the corresponding fluo-

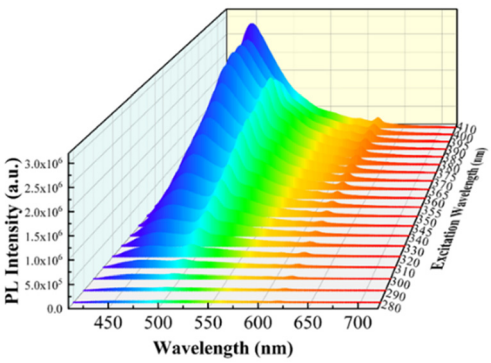

Fig. 7 Excitation wavelength-dependent fluorescence spectra of the Eu/ZIF-L film.

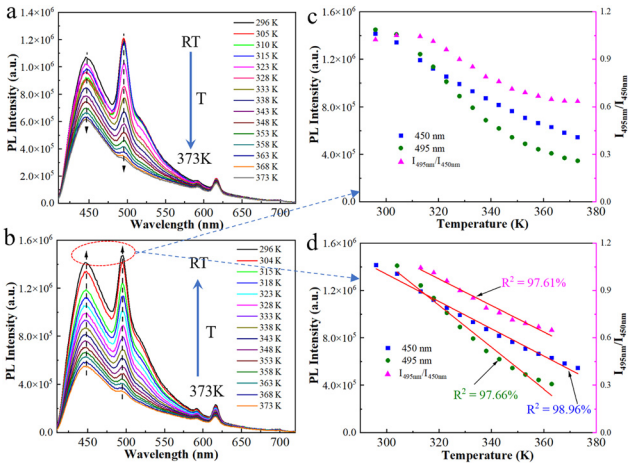

Fig. 8 Fluorescence spectra of the Eu/ZIF-L film over a temperature range of room temperature (23 °C) to 100 °C during processes of increasing temperature (a) and decreasing temperature (b). Experimentally measured and nonlinear-fitted plots (c) and linear-fitted plots (d) of fluorescence intensities of peaks (450 and 495 nm) and relative strength of the two peaks.

rescence peaks gradually increased as the temperature decreased from 100 °C to room temperature (Fig. 8b), suggesting the fluorescence reversibility to temperature. Moreover, fluorescence intensities of the peaks at 450 nm ($I_{450\ nm}$) and 495 nm ($I_{495\ nm}$) quenched by 61.5% and 76.1% at 23–100 °C, as shown in Fig. 8c, respectively.

In Fig. 8d, a relationship of $I_{495\ nm}/I_{450\ nm}$ *versus* temperature (°C) reveals a linear fitting equation: $I_{495\ nm}/I_{450\ nm}$ = −0.0084 T + 3.6617 at 313–363 K with a correlation coefficient R^2 = 97.61%, whose sensitivity was calculated as 1.95% K^{-1} at 363 K. The relationship of emission peaks at 450 and 495 nm *versus* *T* also showed linear fitting equations: $I_{450\ nm}$ = −11 519.7690 T + 4 793 135.0127 (R^2 = 98.96%, 296–373 K, sensitivity: 1.26% K^{-1} at 373 K) and $I_{495\ nm}$ = −17 679.1704 T + 6 731 939.4256 (R^2 = 97.66%, 304–363 K, sensitivity: 1.61% K^{-1} at 363 K). Furthermore, by consulting relevant literature,[52] based on the relative sensitivity (Sr), the temperature resolution of this thermometer could be calculated *via* eqn (1) and (2) as 0.18 K. These results indicate that both the fluorescence peaks and relative intensities of the two emission peaks have a good linear relationship with temperature over a range of temperatures, suggesting a great potential to be used in fluorescence thermal response applications. Additionally, the Eu/ZIF-L film exhibits sufficient sensitivity to temperature, making it suitable for sensing applications in non-contact temperature measurement. By comparing our current work with previously reported MOF-based temperature sensors (Table 1), it is demonstrated that Eu/ZIF-L developed in this study not only has higher sensitivity but also exhibits superior temperature-sensing performance.[4,7,53–57]

3.4. Origins of Eu^{2+} and kinetic insights into ZIF-8-to-ZIF-L structural transformation

3.4.1. Discussion on the source of Eu^{2+}. The generation mechanism of Eu^{2+} in the research system can be clearly attributed to the valence transition of Eu^{3+} under the thermal activation of curing temperature, which leads to the conversion of part of Eu^{3+} to Eu^{2+}. The experimental data show that no characteristic signal of Eu^{2+} is detected in the sol system without heat treatment (Fig. S8a), while the sample treated with 100 °C curing shows an obvious characteristic peak of Eu^{2+} in the XPS spectrum (Fig. 4b, Fig. S5a). Moreover, the characteristic emission peak of Eu^{2+} at 495 nm in the PL spectrum is significantly enhanced with the increase of curing temperature (Fig. S8c and d), which directly confirms that the curing temperature is the core driving force for the conversion of Eu^{3+} to Eu^{2+}.

$$\delta T = \frac{1}{\mathrm{Sr}} \cdot \frac{\delta \mathrm{FIR}}{\mathrm{FIR}} \quad (1)$$

$$\frac{\delta \mathrm{FIR}}{\mathrm{FIR}} = \sqrt{\left\{\frac{\delta I_1}{I_1}\right\}^2 + \left\{\frac{\delta I_2}{I_2}\right\}^2} \quad (2)$$

From the perspective of thermal activation mechanism, the energy provided by the curing temperature can break the stability of the electronic configuration of Eu^{3+}: when the curing temperature rises to a certain value (such as 100 °C in the experiment), the thermal energy of the system promotes Eu^{3+} to obtain electrons to complete the valence band transition, and part of Eu^{3+} is converted into Eu^{2+}. At the same time, during the curing process of the Eu/ZIF-L wet film, Eu^{2+} coordinates with the protonated nitrogen active sites in the ZIF framework, occupies the Zn^{2+} sites, and causes the change of the growth direction of the ZIF structure. The XRD results

Table 1 Comparison of MOF-based temperature sensing performance

Samples	Material system	Temperature range (K)	S_r (K^{-1})	Temperature resolution (K)	Ref.
Eu/ZIF-L	Ln-MOF with multiple luminescent centers	296–373	1.95% (363 K)	0.18	This work
Cdots&RB@ZIF-8²-MMM	MOF–nanocomposite mixed-matrix membrane	293–353	0.74% (293 K)	<0.058	4
Cz-Ant@ZIF-8	Dye emissions within MOF	278–353	1.55% (278 K)	0.39–0.62	7
$Eu_{0.05}Y_{0.95}$-PTC	Dual-luminescence Ln-MOF	303–383	1.94% (383 K)	—	53
ZJU-28 ⊃ ACF	Dye molecules encapsulated in MOF	293–313	0.025% (313 K)	—	54
$EuxTb_{1-x}BPT$	Mixed-lanthanide MOFs	293–353	>1.5%	—	55
MOF@UCNPs	Lanthanide-nanoparticles anchoring on MOF	298–316	1.92% (298 K)	—	56
EuW_{10}/GCDs@ZIF-8²	MOF incorporating polyoxometalates and carbon dots	273–353	1.45% (353 K)	0.29	57

show that the characteristic peak of ZIF-L appears along with the generation of Eu^{2+} (Fig. 1), which also verifies that there is a close relationship between the valence transition induced by thermal activation of curing temperature and the structural phase transition.

3.4.2. Effect of Eu^{2+} concentration on the kinetics of ZIF-8-to-ZIF-L structural transformation. Eu^{2+} concentration plays a crucial role in the structural transformation from ZIF-8 to ZIF-L. Based on the XRD results of a series of Eu concentrations (Fig. S1), when the concentration of $Eu(NO_3)_3{\cdot}6H_2O$ is $\leq$0.033 mol L^{-1}, ZIF-8 is the main phase, with only a weak characteristic peak of ZIF-L appearing at 17.2° (402). When the concentration is $\geq$0.067 mol L^{-1}, the characteristic peak of ZIF-L is significantly enhanced. This indicates that when the concentration of Eu^{2+} in the system is low, its ability to compete with Zn^{2+} for 2-methylimidazole ligands is limited, and the three-dimensional cross-linked structure of ZIF-8 dominates.

With the increase of Eu^{2+} concentration, synchronous XPS analysis shows that the proportion of Eu^{2+} reaches the highest at 0.133 mol L^{-1} (Fig. S5a). More Eu^{2+} forms coordination with protonated N active sites in part of the ZIF structure, and the relative strength of Eu–N bonds also reaches a peak (Fig. S4). Since the ionic radius of Eu^{2+} is larger than that of Zn^{2+} and it tends to have a higher coordination number, this causes a change in the arrangement of ligands. More ligands are arranged in a manner of "intra-layer bridging and inter-layer interaction", gradually inducing the structural transformation from 3D ZIF-8 to 2D ZIF-L.

From a kinetic perspective, the increase in Eu^{2+} concentration is equivalent to increasing the "driving force" for structural transformation in the reaction system. Analogous to the effect of concentration on the reaction rate in chemical reaction kinetics, a higher Eu^{2+} concentration increases the number of effective collisions in the structural transformation, thereby accelerating the rate of transformation from ZIF-8 to ZIF-L. In our experimental observations, as the concentration of Eu salt increases, the intensity of the characteristic diffraction peak of ZIF-L gradually enhances, which indirectly confirms that a higher Eu^{2+} concentration promotes the phase transformation process.

3.4.3. Effect of curing temperature on the kinetics of ZIF-8-to-ZIF-L structural transformation. Curing temperature is also an important factor affecting the kinetics of ZIF-8-to-ZIF-L structural transformation. From the experimental results, only the Eu/ZIF film subjected to 100 °C heat treatment exhibits the ZIF-L phase, while ZIF-L is not detected in the Eu/ZIF sol without heat treatment (Fig. 1, Fig. S8a). This indicates that the curing temperature has a significant impact on the structural transformation from ZIF-8 to ZIF-L.

The increase in curing temperature, on one hand, accelerates the thermal motion of molecules in the system, thereby increasing the reaction rates between Eu^{3+} and ligands, Eu^{2+} and ligands, and Zn^{2+} and ligands. On the other hand, the increase in temperature may affect the reduction rate of Eu^{3+} to Eu^{2+}. The PL spectra (Fig. S8c and d) show that the intensity

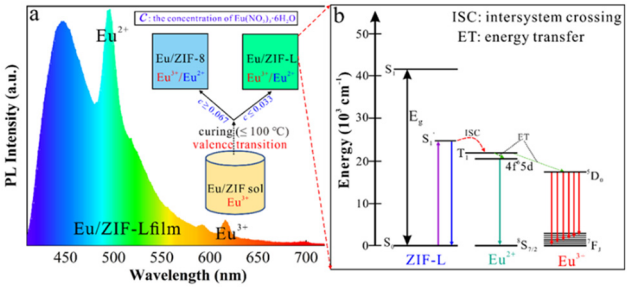

Fig. 9 Schematic illustration of the structure formation (a) and luminescence mechanism (b) for the Eu/ZIF-L film.

at 495 nm (characteristic peak of Eu^{2+}) significantly enhances with the increase of curing temperature, indicating that high temperature promotes the reduction of $Eu^{3+} \rightarrow Eu^{2+}$, thereby increasing the generation amount of Eu^{2+} and providing more "power" for the structural transformation.

In addition, temperature also has a significant impact on the activity of ligands and the stability of metal–ligand coordination bonds. Appropriately increasing the temperature may weaken the strength of Zn–ligand coordination bonds in the original ZIF-8 structure, while enhancing the ability of Eu^{2+} to form coordination bonds with ligands, making the structure more prone to transformation to ZIF-L.

3.5. Structure formation and luminescence mechanism

Following the above test results, we propose possible structure formation mechanisms and luminescence mechanism explanations for the structure and fluorescence properties of the Eu/ZIF-L film, as shown in Fig. 9. $Eu(NO_3)_3{\cdot}6H_2O$ was introduced into the ZIF sol, and europium mainly existed in the sol as Eu(III). The Eu/ZIF sol was spin-coated to form a film, and the wet film was transformed into Eu^{2+} due to the valence band transition of Eu^{3+} in the curing process affected by the temperature, and the Eu^{2+} coordinated with the N-active sites in the ZIF framework occupied some of the protonation sites that had been partially coordinated with Zn^{2+}. On the other hand, the coordination of Eu^{2+} with some of the N active sites in the ZIF-L framework produces an antenna effect, *i.e.*, the electrons in ZIFL absorb photon energy and jump from the ground state (S_0) to the excited state (S'_1), the electrons in the excited state traversed to the single-line triplet state (T'_1) *via* intersystem crossing, and then part of the energy was transferred to Eu^{2+}, which enhanced the fluorescence of Eu^{2+} (495 nm) and formed a strong narrow-band fluorescence emission.

4. Conclusions

Eu/ZIF-L films with multiple emissions were successfully synthesized through introducing small amount of $Eu(NO_3)_3{\cdot}6H_2O$ into a ZIF sol. Controlling the curing temperature of the Eu/ZIF-L film promotes the valence conversion of Eu^{3+} to Eu^{2+},

which actively participates in the formation of the ZIF framework, hence changing the growth direction of the Eu/ZIF film and achieving the phase transformation from 3D ZIF-8 to 2D ZIF-L. The fluorescence peak of Eu^{2+} becomes narrow and strong due to the antenna effect originating from the coordination of Eu^{2+} with N active sites in the ZIF-L skeleton. Under 360 nm excitation, the dual-emission peaks at 450 and 495 nm demonstrate temperature-dependent fluorescence quenching with 61.5% and 76.1% intensity reduction over a broad temperature range from room temperature to 373 K, respectively. Notably, FIR (I_{495}/I_{450}) shows excellent linear correlation with temperature, accompanied by a relative sensitivity of 1.95% K^{-1}. In this sense, the Eu/ZIF-L film with a good reversible fluorescence thermal response performance has great potential for temperature-sensing. In this work, the composite MOF materials prepared by us with the Eu^{3+} ion as a multi-luminescent center show intriguing structural transformations and performance enhancements, which provide new insights for the innovative design of luminescent composites for applications with ratiometric temperature sensing.

Author contributions

Qiufen Liu and Longxiao Zhou conceived experimental ideas and conducted experimental investigations. Jiayu Zheng assisted with experimental investigations and manuscript writing. Senwei Wu and Yuting Peng were responsible for testing and characterization and experimental data analysis. Shouqin Tian and Xiujian Zhao were both involved in the process of supervision and extensive revision of the manuscript.

Conflicts of interest

The authors declare that they have no known competing financial interests or personal relationships that could have appeared to influence the work reported in this paper.

Data availability

The data supporting this article have been included as part of the SI. See DOI: **https://doi.org/10.1039/d5qi01248a**.

Acknowledgements

This work was supported by the National Natural Science Foundation of China (No. 51772229), the National Natural Science Foundation of Hubei Province (No. 2023AFD055) and the National Innovation and Entrepreneurship Training Program for College Students (No. S202410497018). We thank the Analytical and Testing Center of WUT for the help with carrying out XRD, XPS, FESEM and FTIR analyses.

References

1 L. A. Ramolise, S. N. Ogugua, H. C. Swart and D. E. Motaung, Recent advances on visible and near-infrared thermometric phosphors with ambient temperature sensitivity: A review, *Coord. Chem. Rev.*, 2025, **522**, 216196.
2 C. D. S. Brites, R. Marin, M. Suta, A. N. Carneiro Neto, E. Ximendes, D. Jaque and L. D. Carlos, Spotlight on Luminescence Thermometry: Basics, Challenges, and Cutting-Edge Applications, *Adv. Mater.*, 2023, **35**, 2302749.
3 M. Szymczak, D. Szymański, M. Piasecki, M. Brik and L. Marciniak, Luminescence Thermometry Based on Time Gates: Highly Sensitive Approach for Real-Time Sensing and Imaging, *J. Phys. Chem. Lett.*, 2025, **16**, 5960–5970.
4 M. Zheng, L. Li, D. Tian, Z. Zhang, W. Zhou and M. He, Tailoring Dye Emissions within Metal–Organic Frameworks for Tunable Luminescence and Ratiometric Temperature Sensing, *ACS Appl. Mater. Interfaces*, 2023, **15**, 23479–23488.
5 A. Hori, A. Matsumoto, J. Ikenouchi and G.-I. Konishi, D–π–A Fluorophores with Strong Solvatochromism for Single-Molecule Ratiometric Thermometers, *J. Am. Chem. Soc.*, 2025, **147**, 9953–9961.
6 W. Song, W. Ye, L. Shi, J. Huang, Z. Zhang, J. Mei, J. Su and H. Tian, Smart molecular butterfly: an ultra-sensitive and range-tunable ratiometric thermometer based on dihydrophenazines, *Mater. Horiz.*, 2020, **7**, 615–623.
7 Y. Ding, Y. Lu, K. Yu, S. Wang, D. Zhao and B. Chen, MOF-Nanocomposite Mixed-Matrix Membrane for Dual-Luminescence Ratiometric Temperature Sensing, *Adv. Opt. Mater.*, 2021, **9**, 2100945.
8 X. Zhang, Z. Zhu, Z. Guo, Z. Sun and Y. Chen, A ratiometric optical thermometer with high sensitivity and superior signal discriminability based on $Na_3Sc_2P_3O_{12}$: Eu^{2+}, Mn^{2+} thermochromic phosphor, *Chem. Eng. J.*, 2019, **356**, 413–422.
9 Z. Zhu, Z. Sun, Z. Guo, X. Zhang and Z.-C. Wu, A high-sensitive ratiometric luminescent thermometer based on dual-emission of carbon dots/Rhodamine B nanocomposite, *J. Colloid Interface Sci.*, 2019, **552**, 572–582.
10 M. Peng, A. M. Kaczmarek and K. Van Hecke, Ratiometric Thermometers Based on Rhodamine B and Fluorescein Dye-Incorporated (Nano) Cyclodextrin Metal–Organic Frameworks, *ACS Appl. Mater. Interfaces*, 2022, **14**, 14367–14379.
11 P. Kaithrikkovil Varriam and S. Ganesanpotti, Harnessing the Dual-Mode Luminescence of Er/Yb Co-Doped $SrLaLiTeO_6$ Double Perovskite Phosphors for Remarkably Wide Range Temperature Sensing and NIR pc-LEDs, *Laser Photonics Rev.*, 2024, **18**, 2400245.
12 Z. Wang and C. Wang, Excited State Energy Transfer in Metal-Organic Frameworks, *Adv. Mater.*, 2021, **33**, 2005819.
13 W. Cao, Y. Tang, Y. Cui and G. Qian, Energy Transfer in Metal–Organic Frameworks and Its Applications, *Small Struct.*, 2020, **1**, 2000019.
14 L. A. Brandner, B. Marmiroli, M. Linares-Moreau, M. Barella, B. Abbasgholi-Na, M. D. J. Velásquez-

Hernández, K. L. Flint, S. Dal Zilio, G. P. Acuna, H. Wolinski, H. Amenitsch, C. J. Doonan and P. Falcaro, Ordered Transfer from 3D-Oriented MOF Superstructures to Polymeric Films: Microfabrication, Enhanced Chemical Stability, and Anisotropic Fluorescent Patterns, *Adv. Mater.*, 2024, **36**, 2404384.

15 F. Saraci, V. Quezada-Novoa, P. R. Donnarumma and A. J. Howarth, Rare-earth metal–organic frameworks: from structure to applications, *Chem. Soc. Rev.*, 2020, **49**, 7949–7977.

16 S. C. Lal, J. I. N and S. Ganesanpotti, A six-mode optical thermometry rooted from the distinct thermal behavior of $SrLaLiTeO_6$: Mn^{4+}, Eu^{3+} double perovskites and their potential application in wavelength detection, *J. Sci.: Adv. Mater. Devices*, 2023, **8**, 100544.

17 R. Zhang, L. Zhu and B. Yue, Luminescent properties and recent progress in applications of lanthanide metal-organic frameworks, *Chin. Chem. Lett.*, 2023, **34**, 108009.

18 Y. Zhao, Y.-H. Chai, M.-M. Zhai, Q.-Y. Jin, X. Lu, Y.-D. Qiao and L.-F. Ma, New functional metal–organic framework (MOF) based optical thermometer by the post-synthesis doping rare earth ions into MOF, *Chin. Chem. Lett.*, 2025, 111085.

19 H. Guan, M. Qi, L. Shi, W. Liu, L. Yang and W. Dou, Ratiometric Luminescent Thermometer Based on the Lanthanide Metal–Organic Frameworks by Thermal Curing, *ACS Appl. Mater. Interfaces*, 2023, **15**, 18114–18124.

20 G. Khandelwal, N. P. Maria Joseph Raj and S. J. Kim, Zeolitic Imidazole Framework: Metal–Organic Framework Subfamily Members for Triboelectric Nanogenerators, *Adv. Funct. Mater.*, 2020, **30**, 1910162.

21 Y. Li, W. Chen, J. Yin, S. Xia, Y. Jiang, Q. Ge, J. Liu, M. Wang, Z. Hou, Y. Bai and P. Shi, Biomineralized ZIF–8 Encapsulating SOD from Hydrogenobacter Thermophilus: Maintaining Activity in the Intestine and Alleviating Intestinal Oxidative Stress, *Small*, 2024, **20**, 2402812.

22 H. Dai, X. Yuan, L. Jiang, H. Wang, J. Zhang, J. Zhang and T. Xiong, Recent advances on ZIF-8 composites for adsorption and photocatalytic wastewater pollutant removal: Fabrication, applications and perspective, *Coord. Chem. Rev.*, 2021, **441**, 213985.

23 J. Troyano, A. Carné-Sánchez, C. Avci, I. Imaz and D. Maspoch, Colloidal metal–organic framework particles: the pioneering case of ZIF-8, *Chem. Soc. Rev.*, 2019, **48**, 5534–5546.

24 B. Ding, X. Wang, Y. Xu, S. Feng, Y. Ding, Y. Pan, W. Xu and H. Wang, Hydrothermal preparation of hierarchical ZIF-L nanostructures for enhanced CO_2 capture, *J. Colloid Interface Sci.*, 2018, **519**, 38–43.

25 M. Gao, G. Liu, Q. Tan, C. Zhao, G. Chen, R. Zhai, Y. Hua, X. Huang, J. Wang and D. Xu, A novel fluorescent probe for Fe^{3+} detection based on two-dimensional leaf-like structure CDs@ZIF-L, *Microchem. J.*, 2022, **182**, 107868.

26 W. Xue, Q. Zhou, F. Li and B. S. Ondon, Zeolitic imidazolate framework-8 (ZIF-8) as robust catalyst for oxygen reduction reaction in microbial fuel cells, *J. Power Sources*, 2019, **423**, 9–17.

27 X. Chen, X. Jiang, C. Yin, B. Zhang and Q. Zhang, Facile fabrication of hierarchical porous ZIF-8 for enhanced adsorption of antibiotics, *J. Hazard. Mater.*, 2019, **367**, 194–204.

28 R. Chen, J. Yao, Q. Gu, S. Smeets, C. Baerlocher, H. Gu, D. Zhu, W. Morris, O. M. Yaghi and H. Wang, A two-dimensional zeolitic imidazolate framework with a cushion-shaped cavity for CO_2 adsorption, *Chem. Commun.*, 2013, **49**, 9500–9502.

29 Z. Zhong, J. Yao, Z.-X. Low, R. Chen, M. He and H. Wang, Carbon composite membrane derived from a two-dimensional zeolitic imidazolate framework and its gas separation properties, *Carbon*, 2014, **72**, 242–249.

30 S. Li, S. Qi, K. Liu, H. Yuan and X. Sun, Influence of nitridation on optical properties of $Sr_2MgSi_2O_7$:Eu^{2+} phosphors, *Ceram. Int.*, 2019, **45**, 20967–20971.

31 X. Li, Y. Hua, H. Ma, D. Deng and S. Xu, Modification of the crystal structure of $Sr_{2-x}Ba_xSi(O,N)_4$: Eu^{2+} phosphors to improve their luminescence properties, *CrystEngComm*, 2015, **17**, 9123–9134.

32 Q. Liu, S. Tian, X. Zhao and G. Sankar, An enhanced fluorescent ZIF-8 film by capturing guest molecules for light-emitting applications, *J. Mater. Chem. C*, 2021, **9**, 5819–5826.

33 I. J. Villar-Garcia, E. F. Smith, A. W. Taylor, F. Qiu, K. R. J. Lovelock, R. G. Jones and P. Licence, Charging of ionic liquid surfaces under X-ray irradiation: the measurement of absolute binding energies by XPS, *Phys. Chem. Chem. Phys.*, 2011, **13**, 2797–2808.

34 W. Shi, S. Zhang, Y. Wang, Y. D. Xue and M. Chen, Preparation of dual-ligands Eu-MOF nanorods with dual fluorescence emissions for highly sensitive and selective ratiometric/visual fluorescence sensing phosphate, *Sens. Actuators, B*, 2022, **367**, 132008.

35 W. Shi, T. Li, N. Chu, X. Liu, M. He, B. Bui, M. Chen and W. Chen, Nano-octahedral bimetallic Fe/Eu-MOF preparation and dual model sensing of serum alkaline phosphatase (ALP) based on its peroxidase-like property and fluorescence, *Mater. Sci. Eng., C*, 2021, **129**, 112404.

36 J. Rocha, C. D. S. Brites and L. D. Carlos, Lanthanide Organic Framework Luminescent Thermometers, *Chem. – Eur. J.*, 2016, **22**, 14782–14795.

37 N. Li, L. Zhou, X. Jin, G. Owens and Z. Chen, Simultaneous removal of tetracycline and oxytetracycline antibiotics from wastewater using a ZIF-8 metal organic-framework, *J. Hazard. Mater.*, 2019, **366**, 563–572.

38 J. Wang and L. Xiang, Formation of ZnO rods with varying diameters from ε-$Zn(OH)_2$, *J. Cryst. Growth*, 2014, **401**, 279–284.

39 C. Huang, H. Zhang, K. Zheng, Z. Zhang, Q. Jiang and J. Li, Two-dimensional hydrophilic ZIF-L as a highly-selective adsorbent for rapid phosphate removal from wastewater, *Sci. Total Environ.*, 2021, **785**, 147382.

40 Z. Zhong, J. Yao, R. Chen, Z. Low, M. He, J. Z. Liu and H. Wang, Oriented two-dimensional zeolitic imidazolate framework-L membranes and their gas permeation properties, *J. Mater. Chem. A*, 2015, **3**, 15715–15722.

41 A. Zurawski, M. Mai, D. Baumann, C. Feldmann and K. Müller-Buschbaum, Homoleptic imidazolate frameworks $^{3}\infty[Sr_{1-x}\ Eu_x(Im)_2]$—hybrid materials with efficient and tuneable luminescence, *Chem. Commun.*, 2011, **47**, 496–498.

42 J.-C. Rybak, M. Hailmann, P. R. Matthes, A. Zurawski, J. Nitsch, A. Steffen, J. G. Heck, C. Feldmann, S. Götzendörfer, J. Meinhardt, G. Sextl, H. Kohlmann, S. J. Sedlmaier, W. Schnick and K. Müller-Buschbaum, Metal-Organic Framework Luminescence in the Yellow Gap by Codoping of the Homoleptic Imidazolate $\infty^3[Ba(Im)_2]$ with Divalent Europium, *J. Am. Chem. Soc.*, 2013, **135**, 6896–6902.

43 M. T. Abbas, M. Szymczak, V. Kinzhybalo, M. Drozd and L. Marciniak, NIR-to-NIR Lifetime Based Thermometry with the Thermally Elongated Luminescence Kinetics Driven by Structural Phase Transition in $LiYO_2$:Yb^{3+}, *Laser Photonics Rev.*, 2025, **19**, 2401108.

44 J. Baltrusaitis, P. M. Jayaweera and V. H. Grassian, XPS study of nitrogen dioxide adsorption on metal oxide particle surfaces under different environmental conditions, *Phys. Chem. Chem. Phys.*, 2009, **11**, 8295–8305.

45 F. Mercier, C. Alliot, L. Bion, N. Thromat and P. Toulhoat, XPS study of Eu(III) coordination compounds: Core levels binding energies in solid mixed-oxo-compounds $Eu_mX_xO_y$, *J. Electron Spectrosc. Relat. Phenom.*, 2006, **150**, 21–26.

46 G. Zhao, H. Wu, R. Feng, D. Wang, P. Xu, H. Wang, Z. Guo and Q. Chen, Bimetallic Zeolitic Imidazolate Framework as an Intrinsic Two-Photon Fluorescence and pH-Responsive MR Imaging Agent, *ACS Omega*, 2018, **3**, 9790–9797.

47 Z. Zhou, M. Shang, Z. Yao and J. Zhang, Eu-MOF fluorescent fiber detector based on polyacrylonitrile: A highly selective and sensitive luminescence sensor for trace amounts of Fe^{3+}, *Dyes Pigm.*, 2022, **198**, 110016.

48 J. Qiao and Z. Xia, Design principles for achieving red emission in Eu^{2+}/Eu^{3+} doped inorganic solids, *J. Appl. Phys.*, 2021, **129**, 200903.

49 J.-Q. Liu, Z.-D. Luo, Y. Pan, A. Kumar Singh, M. Trivedi and A. Kumar, Recent developments in luminescent coordination polymers: Designing strategies, sensing application and theoretical evidences, *Coord. Chem. Rev.*, 2020, **406**, 213145.

50 A. Herrmann, S. Fibikar and D. Ehrt, Time-resolved fluorescence measurements on Eu^{3+}- and Eu^{2+}-doped glasses, *J. Non-Cryst. Solids*, 2009, **355**, 2093–2101.

51 Z. Yang, G. Liu, Y. Zhao, Y. Zhou, J. Qiao, M. S. Molokeev, H. C. Swart and Z. Xia, Competitive Site Occupation toward Improved Quantum Efficiency of $SrLaScO_4$:Eu Red Phosphors for Warm White LEDs, *Adv. Opt. Mater.*, 2022, **10**, 2102373.

52 M. Back, J. Ueda, J. Xu, D. Murata, M. G. Brik and S. Tanabe, Ratiometric Luminescent Thermometers with a Customized Phase-Transition-Driven Fingerprint in Perovskite Oxides, *ACS Appl. Mater. Interfaces*, 2019, **11**, 38937–38945.

53 Q. Sun, X. Sui, Q.-Y. Zhu, S.-S. Zhu, X.-S. Gao and X.-M. Ren, Ln-MOF and its hydrogel composite Ln-MOF@PVA for dual-luminescence ratiometric temperature sensing, *Inorg. Chem. Commun.*, 2023, **158**, 111571.

54 S. Lin, Z. Liao, H. Zheng, C. Li, Y. Cui, Z. Wang and G. Qian, A polarized luminescence thermometer based on a dye encapsulated metal–organic framework, *J. Mater. Chem. C*, 2024, **12**, 2391–2397.

55 Y. X. Lin Zhang, T. Xia, Y. Cui, Yu Yang and G. Qian, A highly sensitive luminescent metal–organic framework thermometer for physiological temperature sensing, *J. Rare Earths*, 2018, **36**, 561–566.

56 W. Cao, Z. Liao, H. Chen, Y. Cui, Z. Wang and G. Qian, Lanthanide-Doped Nanoparticles Anchoring on Metal–Organic Frameworks with Thermally Enhanced Upconversion Luminescence for Sensitive Nanothermometers, *ACS Appl. Mater. Interfaces*, 2024, **16**, 58920–58930.

57 C. Viravaux, P. Mialane, A. Dolbecq, N. Ramsahye, C. Mellot-Draznieks, H. Serier-Brault and O. Oms, Tunable ratiometric temperature sensors based on a Zn-MOF material incorporating luminescent polyoxometalates and carbon dots, *J. Mater. Chem. C*, 2024, **12**, 15535–15540.

